Int. J. Heat Mass Transfer. Vol. 33, No. 6, pp. 1193–1204, 1990
Printed in Great Britain

0017–9310/90 $3.00 + 0.00
© 1990 Pergamon Press plc

Numerical computations of steady transonic and supersonic flow fields

A. PALACIO
Institute of Engineering, National University of Mexico, Ciudad Universitaria, Coyoacan, 04510, Mexico, D.F., Mexico

M. R. MALIN and N. PROUMEN
CHAM Limited, Bakery House, Wimbledon, London SW19 5AU, U.K.

and

L. SANCHEZ
Thames Polytechnic, School of Mathematics, Statistics and Computing, Wellington Street, Woolwich SE18, U.K.

(*Received* 5 *June* 1989 *and in final form* 14 *August* 1989)

Abstract—A prediction procedure for computing the shock and expansion waves associated with transonic and supersonic flow is presented. In order to assess the capability of the model, calculations are carried out for a number of benchmark cases, for which analytical solutions or published data are available. The cases considered are: supersonic flow over jet vanes; transonic shocked flow in a nozzle; over- and under-expanded free jets with Mach disc formation; and supersonic flow in a cascade of wedges with shock reflection and Prandtl–Meyer expansion. The model, which includes the solution of the steady-state Euler equations as well as the full Navier–Stokes equations, utilizes some modifications made to an existing finite-volume formulation in order to ensure momentum and energy conservation through the shock waves. In all the cases, the calculations compare favourably with the analytical and experimental results.

1. INTRODUCTION

THE APPLICATION of transonic and supersonic flows is found in high technology fields, and the use of numerical methods for their simulation has advanced markedly over the past 10 years. A large number of computational methods have been proposed for the solution of these flows, and an increasing number of them concern the solution of the full compressible Navier–Stokes equations [1–12]. Euler methods have been applied extensively to the prediction of shock waves, and most of them are based on a time-marching approach, whereby steady-state solutions are obtained as the asymptotic limit of an unsteady flow calculation. For steady flow, there exists the alternative of solving the steady-state equations directly by an iterative method.

The present work considers the validation of a steady-state solution algorithm for a series of transonic and supersonic test cases, including both bounded and unconfined flow. Modifications are made to an existing first-order finite-volume formulation in order to ensure momentum and energy conservation through shock waves; these are particularly important in confined flows where they lead to an accurate prediction of the shock position and strength. The smearing effects, which according to the literature are a characteristic feature of shock-capturing methods which employ first-order discretizing schemes, are greatly reduced and virtually eliminated by using an appropriate grid distribution for external flow problems.

Although the full Navier–Stokes equations are solved for some of the cases presented here, the paper focuses on inviscid, transonic and supersonic solutions of the steady-state Euler equations. The motivation is that a reliable calculation of inviscid flow is a prerequisite even if the ultimate objective is to solve the Navier–Stokes equations. Furthermore, it allows direct comparison between the predictions and existing analytical solutions.

The main objective of the work is to investigate the ability of the present prediction procedure for computing the shock and expansion waves associated with transonic and supersonic flow fields. The remainder of the paper is divided in three sections. Section 2

NOMENCLATURE

A_i	coefficients of the finite-volume equation
A_P	central coefficient of the finite-volume equations
a	acoustic velocity
c	chord
$C_{D,fr}$	drag coefficient due to friction
$C_{D,sh}$	drag coefficient due to shock
$C_{D,tot}$	total drag coefficient
D_D	diameter of the Mach disc
D_N	diameter of the jet nozzle
h	static enthalpy
I	unit tensor
k	turbulent kinetic energy
L	reference length
M	local Mach number
M_w	molecular weight of the gas
p	static pressure
P_k	stress-production rate of k
$\mathbf{Q}^m$	molecular heat-flux vector
$\mathbf{Q}^t$	turbulent heat-flux vector
S_Φ	integral source term
T^m	molecular stress tensor
T^t	turbulent stress tensor
$\mathbf{U}$	velocity vector
x	axial distance
x_D	axial location of the Mach disc from nozzle
x_s	shock location.

Greek symbols

α	wedge-profile deflection angle
δ	wedge-profile thickness ratio
ε	dissipation rate of the kinetic energy
γ	specific heat ratio
μ	fluid dynamic viscosity
ρ	fluid density
σ_h	molecular Prandtl number
$\sigma_{h,t}$	turbulent Prandtl number
Φ	dependent variable.

Subscripts

A	ambient condition
e	exit condition
i	value at the inflow boundary
N	nozzle discharge condition
P	value at the node
t	turbulent
0	total condition
0, i	inflow boundary under total conditions.

Other symbols

$\otimes$	dyadic product
:	tensor product.

outlines the mathematical model and describes the solution procedure. Section 3 describes and discusses the solutions obtained for the various applications, and in Section 4 the concluding remarks are made together with some recommendations for future work.

2. MATHEMATICAL MODEL

2.1. *Conservation equations*

In general, the flows considered here are assumed to be compressible, steady and turbulent. Turbulence is represented by the statistical approach, whereby the conservation equations are achieved as the statistical average of the decomposition of dependent variables into a mean part and a turbulent fluctuating part. Neglecting body forces, the resulting statistically-averaged conservation equations of mass, momentum and energy can be expressed in coordinate-free form as follows:

continuity

$$\nabla\cdot(\rho\mathbf{U}) = 0; \tag{1}$$

momentum

$$\nabla\cdot(\rho\mathbf{U}\otimes\mathbf{U}) = -\nabla p+\nabla\cdot(T^m+T^t); \tag{2}$$

energy

$$\nabla\cdot(\rho\mathbf{U}h) = -\nabla\cdot(\mathbf{Q}^m+\mathbf{Q}^t)+\mathbf{U}\cdot\nabla p +(T^m+T^t):\nabla\mathbf{U} \tag{3}$$

where all symbols are defined in the Nomenclature.

The density of the fluid is determined from an equation of state, which for the present applications is taken in perfect-gas form as

$$p = \frac{\gamma-1}{\gamma}\rho h. \tag{4}$$

The molecular stress tensor and the molecular flux vectors are computed from the following relationships:

$$T^m = 2\mu D-\tfrac{2}{3}[\mu\nabla\cdot\mathbf{U}]I \tag{5}$$

$$Q^m = -\frac{\mu}{\sigma_h}\nabla h \tag{6}$$

where the deformation tensor D is given by

$$D = \tfrac{1}{2}[\nabla\mathbf{U}+(\nabla\mathbf{U})^\dagger] \tag{7}$$

where the superscript † denotes that the transpose of the dyadic $\nabla\mathbf{U}$ is taken. In turbulent flows of sufficiently high Reynolds number, the molecular terms are negligible compared with their turbulent counterparts except in the close vicinity of walls.

2.2. *Turbulence modelling*

The averaging approach employed here adopts a density weighting of the velocity and other dependent variables except pressure and density, so that these variables are decomposed into the sum of a density-weighted mean plus a corresponding fluctuation [13]. In direct analogy to laminar flows, the turbulent stress tensor and turbulent flux vectors are computed from the following closure models:

$$T^t = 2\mu_t D - \tfrac{2}{3}[\mu_t \nabla \cdot \mathbf{U} + \rho k]I \tag{8}$$

$$\mathbf{Q}^t = -\frac{\mu_t}{\sigma_{h,t}} \nabla h. \tag{9}$$

Thus, turbulent transport is modelled by using the Boussinesq stress–strain relation, which relates the Reynolds stresses to the mean strain field by the use of an isotropic eddy viscosity.

For the calculations presented in this study, the turbulent viscosity μ_t is determined from the high-Reynolds-number form of the two-equation k–ε turbulence model (see, for example, Rodi [14]).

The turbulent kinetic energy and its dissipation rate are obtained by solving the following modelled transport equations:

$$\nabla \cdot (\rho \mathbf{U} k) = \nabla \cdot (\Gamma_k \nabla k) + P_k - \rho\varepsilon \tag{10}$$

$$\nabla \cdot (\rho \mathbf{U} \varepsilon) = \nabla \cdot (\Gamma_\varepsilon \nabla \varepsilon) + \frac{\varepsilon}{k}(C_{1\varepsilon} P_k - \rho C_{2\varepsilon} \varepsilon) \tag{11}$$

where the stress-production rate of k, P_k, is defined by

$$P_k = T^t : \nabla \mathbf{U} \tag{12}$$

and Γ_k and Γ_ε are exchange coefficients for k and ε, respectively

$$\Gamma_k = \mu + \mu_t/\sigma_k\,; \quad \Gamma_\varepsilon = \mu + \mu_t/\sigma_\varepsilon. \tag{13}$$

The turbulence-model coefficients σ_k, σ_ε, $C_{1\varepsilon}$ and $C_{2\varepsilon}$ are assigned the constant values of 1.0, 1.314, 1.44 and 1.92 respectively, as recommended by Launder and Spalding [15]. Although molecular transport has been allowed for in the diffusive transport terms, the form of the k–ε model used here is essentially the high-Reynolds-number version. However, the model may be extended to include low-Reynolds-number effects, as done for example by Jones and Launder [16] and Lam and Bremhorst [17].

No attempt has been made in the present study to include compressibility terms in the k–ε model because there appears to be no modelling approximations that could be claimed to be ready for widespread application. In fact, the experiences of other groups (see, for example, Vandromme and HaMinh [18]) with modelling the compressibility terms indicate that in most applications they have little influence on the quality of the predictions. However, this particular aspect may warrant further investigation when strong shock waves are present in the flow field, and especially when the shock waves are strong enough to cause separation.

2.3. *Euler limit equations*

In the present work, inviscid calculations are also made by using the so-called Euler form of the full-field equations. These equations are obtained by applying the Euler limit operators ($\mu \to 0$; $\mu_t \to 0$) to the conservation equations and dispensing with the turbulence-model transport equations.

2.4. *Dimensionless flow variables*

So as to allow a direct computation of dimensionless flow variables, the foregoing equations are normalized [19] by introducing the following reference values:

$$\text{length}: L;\ \text{density}: \rho_{0,i};$$

$$\text{velocity}: \frac{a_{0,i}}{\sqrt{\gamma}};\ \text{pressure}: p_{0,i};$$

$$\text{enthalpy}: \frac{\gamma - 1}{\gamma} h_{0,i};\ \text{turbulence energy}: \frac{a_{0,i}^2}{\gamma};$$

$$\text{dissipation rate}: \frac{a_{0,i}^3}{\gamma\sqrt{\gamma L}};$$

$$\text{turbulent kinematic viscosity}: \frac{a_{0,i} L}{\sqrt{\gamma}}. \tag{14}$$

2.5. *The finite-volume equations*

The solution domain is sub-divided into a number of control volumes, each associated with a grid point, while the velocities are stored at staggered locations which lie between the pressure nodes. The control volumes for the velocities are staggered in relation to the control volumes for scalar variables. The finite-volume equations for each variable are derived by a control volume approach with the aid of assumptions about the distribution of the variables between nodes centred in each control volume. For the convection terms, all fluid properties are assumed uniform over cell faces; and, except in respect of the velocities for which the face-centre values are stored, the values prevailing at the cell face are determined by using upwind interpolation.

For any dependent variable, the partial differential equation is represented by a coupled set of algebraic equations of the form

$$A_P \Phi_P = \sum_i A_i \Phi_i + S_\Phi \tag{15}$$

where the A_i's are the coefficients expressing the influence of convection, S_Φ is the integral source term and the summation sign Σ stands for summation over the neighbouring nodes. A complete statement of the finite-volume equations is given by Rosten and Spalding [20], although the present work modifies their original momentum–convection formulation in order

to ensure momentum conservation through a shock wave [19].

2.6. *Solution procedure*

The solution algorithm is based upon the iterative 'guess-and-correct' procedure of Patankar and Spalding [21], but is modified in accordance with the SIMPLEST algorithm [22]. First, the equation of state is solved and then a modified version of Stone's strongly implicit method [23] is used to solve the enthalpy equation. Next, the velocities are obtained by solving the momentum equations using the old iterate pressures. The solution for the velocity variables proceeds by way of the SIMPLEST procedure. Then, continuity is enforced by solving a pressure-correction (p') equation [24], which determines the required adjustments to the velocities and pressures. A compressible form of the p'-equation is employed. The equation is developed by utilizing: the equation of state, source terms from the finite-volume continuity equation, and coefficients from truncated forms of the momentum equations. The p'-equation is solved in a 'whole-field' manner by using a simultaneous procedure, which is also similar to Stone's method. The whole process is then repeated until the solution converges. More detailed descriptions of the solution algorithm and its features can be found in refs. [12, 21, 22, 24].

2.7. *Boundary conditions*

In the present work, the flow can be bounded by an inflow boundary, a downstream outflow boundary, a free boundary, a cyclic boundary, a solid wall, and a symmetry plane. In general, the inflow conditions depend on the flow considered and therefore their definition will be deferred until the problem specifications given in Section 3. The different types of boundary conditions are now described.

At a solid surface, a zero-flux condition is used for inviscid calculations. For turbulent viscous flows, the wall-function approach outlined by Rodi [14] is adopted, which in effect means that the boundary conditions are not specified right at the wall but at a point outside the viscous sub-layer where the logarithmic law of the wall prevails and the turbulence can usually be assumed to be in local equilibrium. A zero-flux condition is applied for the static enthalpy. The boundary conditions for k and ε are also specified at the first grid point where the logarithmic law of the wall is applied.

The wall-function boundary conditions, which are used mainly to economize on computer requirements, are based on the dynamics of incompressible forced-flow boundary layers, and they are not strictly appropriate for high-speed compressible flows. Refinements have been introduced by other workers (see, for example, Viegas and Rubesin [25]) in applying wall-functions to shock/boundary-layer interactions, but such extensions are considered beyond the scope of the present study.

At free boundaries, a fixed pressure condition is employed for subsonic flow regions. For regions of unconfined and supersonic flow, the specified conditions avoid the occurrence of shock reflection and, therefore, they allow waves to pass through the boundary. The boundary condition is formulated in terms of a prescribed mass efflux, ρV, which is defined as follows:

$$\rho V = \frac{\rho(P-P_\infty)}{\rho_\infty W_\infty}(M_\infty^2-1)^{1/2} \tag{16}$$

where W is the axial velocity, V the lateral velocity, M the Mach number and the subscript ∞ denotes free-stream conditions. The origin of this expression comes from the theory of simple wave flow. For the complete derivation of equation (16), the reader is referred to Palacio and Malin [26]. In their work, this boundary condition proved successful at avoiding wave reflection or disturbance at the free-stream boundaries.

On cyclic boundaries, such as those found on the free boundaries upstream and downstream of a blade row, periodicity conditions are applied so that flow properties are identical at corresponding points.

At symmetry planes, the normal gradients for all dependent variables are zero. Consequently, a zero-flux condition is applied along this boundary.

At the outlet boundary, the static pressure is specified and held constant at a value equal to the undisturbed static pressure, which is physically correct as long as the axial Mach number is subsonic. For supersonic outflow, a refined treatment employing a zero-gradient condition for the axial velocities produced very little difference in the results.

3. PRESENTATION AND DISCUSSION OF THE RESULTS

3.1. *Preliminary remarks*

The purpose of this section is to demonstrate the ability of the mathematical model to predict normal and oblique shock waves for a number of benchmark test cases, for which analytical solutions or published data are available. Five text cases are presented in the following order: supersonic flow over a jet vane; transonic shocked flow in a nozzle; over- and under-expanded free jets with Mach disc formation; and supersonic flow in a cascade of wedges with oblique shock reflection and Prandtl–Meyer expansion.

3.2. *Supersonic flow past a jet vane*

The general problem considered is steady, two-dimensional, turbulent, supersonic flow past aerodynamic jet vanes at several incidence angles. First, a double-wedge profile at zero incidence is considered in order to assess the ability of the model to predict the flow downstream of an oblique shock at several incident Mach numbers and deflection angles. Next, the inviscid results obtained for a double-wedge vane

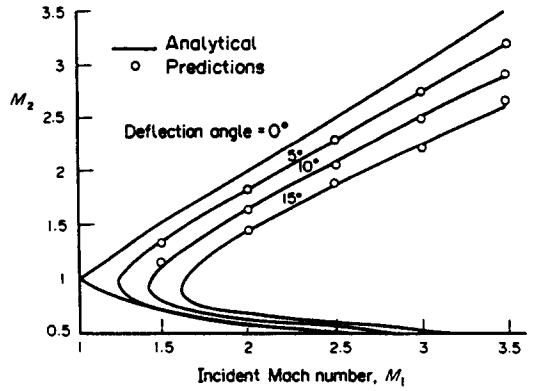

FIG. 1. Post-shock Mach number as a function of incident Mach number and deflection angle.

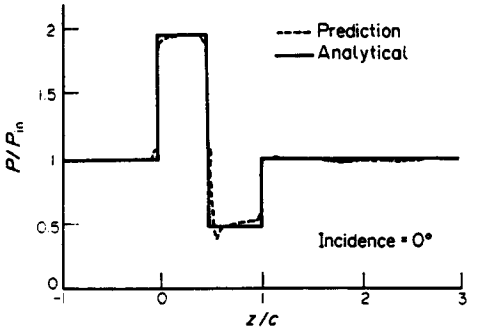

FIG. 3. Normalized static pressure distribution along the double-wedge surface.

design at two incidence angles are compared with the existing analytical solutions, and then viscous effects are included and their influence on the numerical solutions discussed.

3.2.1. *Oblique shocks on a double-wedge profile.* The section has a chord of 4 units, and only half of the profile is considered due to flow symmetry. The lateral extent of the solution domain is 2.5 chords, the inflow boundary is located 0.25 chords upstream of the leading edge, and the outflow boundary is located 6.95 chords downstream of the trailing edge. Inviscid calculations are made for deflection angles, α, ranging from 5° to 15°, and incident Mach numbers ranging from 1.5 to 3.5. For all conditions, the deflection angle is less than the critical value for the approach Mach number, so that the leading-edge shock is always attached. The calculations are performed on a mesh with 110 non-uniformly distributed cells in the main flow direction and 30 cells in the lateral direction.

For the leading-edge oblique shock, Figs. 1 and 2 show the post-shock Mach number and static pressure ratio as a function of the incident Mach number and deflection angle. It can be seen that the numerical predictions are in fairly good agreement with the analytical solutions for all the conditions considered.

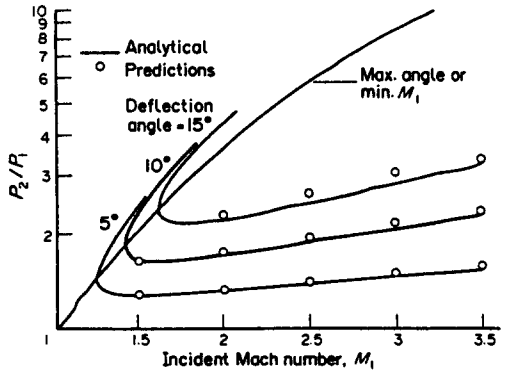

FIG. 2. Static pressure ratio as a function of incident Mach number and deflection angle.

3.2.2. *Effect of incidence angle on a vane design.* To show the effect of the incidence angle on the calculation of the pressure distribution along the surface of the profile, a double-wedge vane design with a chord, c, of 3 units, a deflection angle, α, of 12.12°, and a thickness ratio, δ, of 0.2146 is considered. For this case, the following fluid properties are employed: $\mu = 5.42 \times 10^{-5}$ N s m^{-2}, $\gamma = 1.23$, $M_w = 25.1$ kg kg-mol^{-1}, and $\sigma_h = 0.6$.

The inlet free-stream flow conditions may be summarized as follows: $M_i = 2.5$, $p_0 = 100$ bar, $T_0 = 2660$ K. These values permit the inlet fluxes of mass, momentum and static enthalpy to be determined for use in the numerical computations. The inlet turbulent kinetic energy is specified by taking the turbulent intensity to be 1% of the inlet mean velocity. The inlet dissipation rate is specified by assuming a free-stream eddy viscosity equal to the laminar viscosity from which the free-stream value of ε follows as $\varepsilon = \rho C_\mu k^2/\mu_t$, where $C_\mu = 0.09$.

I. Inviscid calculations

Calculations were performed for the double-wedge profile at 0° and 10° incidence angles. Initially, the Euler equations were solved in order to compare the results with those obtained from inviscid shock-expansion theory (see, for example, Shapiro [27]).

Figure 3 compares the analytical and predicted static pressure distributions along the surface of the vane at zero incidence. The pressure is normalized by the inlet static pressure, and the axial distance is normalized with respect to the chord. It can be seen from the figure that the predictions are in very good agreement with the analytical results. The calculated drag coefficient is 6% lower than the analytical value. Obviously, the lift and moment coefficients are zero for this case.

The static pressure contours around the double-wedge are presented in Fig. 4, and the corresponding Mach number contours are shown in Fig. 5. Both contour plots reveal the expected flow structure; two oblique shocks are generated at the leading edge which diminish in strength with distance from the profile. Two oblique shock waves emanate from the trailing

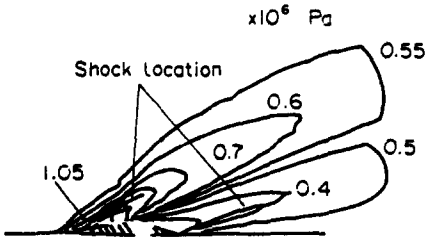

FIG. 4. Pressure contours around the double-wedge profile indicating the shock location.

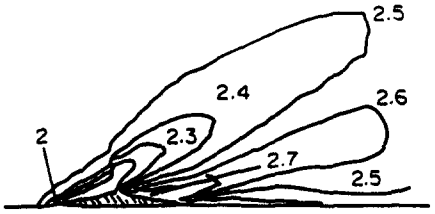

FIG. 5. Mach number contours around the double-wedge profile.

edge of such strength that the flow is restored to the static ambient pressure, as may be noted from Fig. 3. In Figs. 4 and 5, a small discontinuity in the pressure and Mach number contours may be discerned near the middle of the vane. This feature may be a consequence of the rapidly varying cell sizes in this region, as Palacio and Malin [26] predicted smooth contours when employing a uniformly-distributed mesh.

For an incidence angle of 10°, the analytical and predicted static pressure distributions along the upper and lower surfaces of the vane are shown in Fig. 6. The values are normalized as in the previous case. In general it can be seen that the agreement between the numerical and analytical results is very good. The major discrepancy with the theory concerns the strong shock forming on the lower surface, where the model overpredicts the static pressure ratio. The weak shock

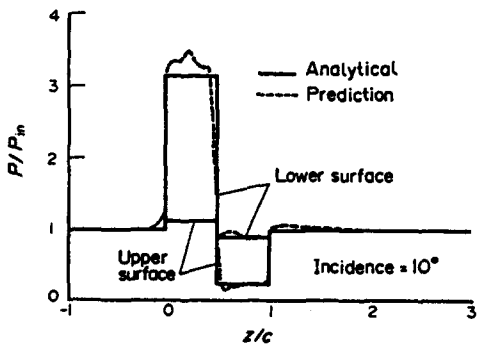

FIG. 6. Normalized static pressure distribution along the surface at 10° incidence.

on the upper surface is very well represented, as are the expansions and trailing-edge shocks on both surfaces.

The calculated drag, lift and moment coefficients are within 10% of the corresponding analytical values. Table 1 provides a summary of the analytical and computed coefficients for both cases. A negative sign for the moment coefficient indicates a clockwise torque acting on the vane.

The static pressure and Mach number contours are presented in Figs. 7 and 8, respectively. The first of these figures clearly shows the maximum pressure on the front lower surface, while the front upper surface is at a pressure only slightly higher than the inlet value; this is due to the small deflection angle of 2°, which gives a very weak shock. From Fig. 8 it can be seen that the maximum Mach number occurs on the rear part of the upper surface, where the largest expansion takes place.

II. Viscous calculations

The effect of viscosity on the calculations was also investigated. The general results of these simulations may be summarized as follows. The total drag coefficient increased due to viscous effects, with the model predicting a skin-friction drag coefficient of about 0.0065 for both cases, which is very close to the typical value of 0.005 quoted by Shapiro [27]. For the second case, the lift coefficient due to friction was negative as may be expected from the orientation of the friction surfaces. However, the total value of the lift remained practically unchanged, which is due to the very small effect of viscous dissipation on these profiles performing in supersonic flow.

The velocity profiles differed basically in the region surrounding the trailing edge, where a very small recirculation zone appeared. The pressure and Mach number contours showed no significant difference when compared to the inviscid results presented earlier in Figs. 7 and 8. In this flow, the boundary layer tends to remain very thin, and is perhaps not resolved adequately in the present calculations. For example, the surface Mach number is typically 2.5 upstream of the trailing edge, which corresponds to a dimensionless wall coordinate y^+ of approximately 1000 at the near-wall grid point.

If the boundary-layer is resolved sufficiently, it may be necessary to switch to a low-Reynolds-number treatment as the wall-function approach cannot really account for very large mechanical dissipation in a very satisfactory way (see, for example, Villasenor and Radosavljevic [28]). However, the influence of viscosity is known to be negligible in the present case, and so refinements in this area are probably not worthwhile.

3.3. *Transonic flow in a nozzle*

The problem considered is one-dimensional transonic flow through the de Laval nozzle of Malin [29]. The nozzle was designed to produce a linear variation of Mach number with axial distance under isentropic

Table 1. Aerodynamic coefficients

	0° incidence			10° incidence		
	Inviscid		Viscous	Inviscid		Viscous
	Prediction	Analytical	Prediction	Prediction	Analytical	Prediction
$C_{D,sh}$	7.62×10^{-2}	8.1×10^{-2}	7.71×10^{-2}	0.154	0.145	0.155
$C_{D,fr}$	0	0	8.16×10^{-3}	0	0	6×10^{-3}
$C_{D,tot}$	7.62×10^{-2}	8.1×10^{-2}	8.53×10^{-2}	0.154	0.145	0.161
$C_{L,sh}$	0	0	0	0.350	0.323	0.352
$C_{L,fr}$	0	0	0	0	0	-9×10^{-4}
$C_{L,tot}$	0	0	0	0.350	0.323	0.351
$C_{M,sh}$	0	0	0	-9.3×10^{-2}	-8.3×10^{-2}	-9.5×10^{-2}
$C_{M,fr}$	0	0	0	0	0	1.6×10^{-4}
$C_{M,tot}$	0	0	0	-9.3×10^{-2}	-8.3×10^{-2}	-9.5×10^{-2}

C_D, drag coefficient; C_L, lift coefficient; C_m, moment coefficient; sh, shock; fr, friction; tot, total.

conditions. For the design case, the flow is asymmetric about the throat with subsonic axial inflow and supersonic outflow. The nozzle has a chord of 3 units and a throat area of 0.25 square units. The inlet Mach number is 0.5 and the design outlet Mach number is 2.0.

Inviscid calculations are made for four different back pressures, three of which produce shocked flow and one of which produces transonic shock-free flow. The results of these calculations are shown in Fig. 9 in terms of the computed distributions of Mach number along the nozzle. The figure shows that in all cases the predictions are in excellent agreement with the theory. The shock position and strength, and exit Mach number (and hence the stagnation-pressure loss) are predicted almost exactly. From the figure it can also be seen that the shock discontinuity is smeared out to be represented by a monotonic transition over several mesh intervals. The solutions for shocked flow required about 400 uniformly-distributed cells to give substantially grid-independent results. Of course, a more economical solution could have been obtained by employing local grid refinement in the vicinity of the shock wave only. The computed normalized mass flow rate through the nozzle is 0.1714, which agrees very well with the analytical value of 0.1712.

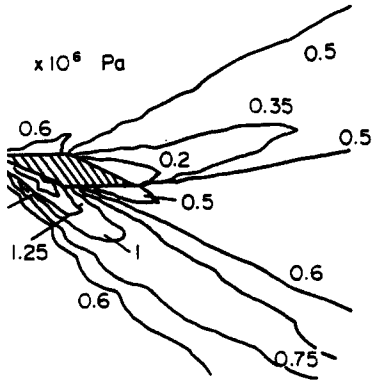

FIG. 7. Pressure contours around the vane.

3.4. *Overexpanded free jets*

The problem considered is an axisymmetric supersonic jet discharging into stagnant surroundings from a nozzle at a pressure less than the ambient pressure. For a discharge Mach number of 2, inviscid calculations are made for static pressure ratios between 0.4 and 0.6, this being the range in which Mach discs

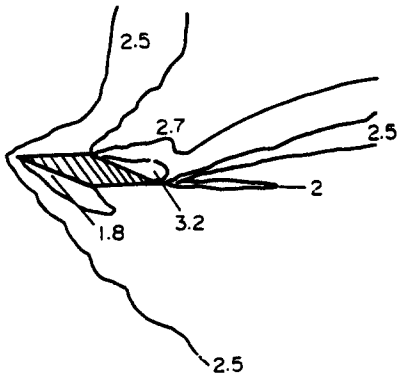

FIG. 8. Mach number contours around the vane.

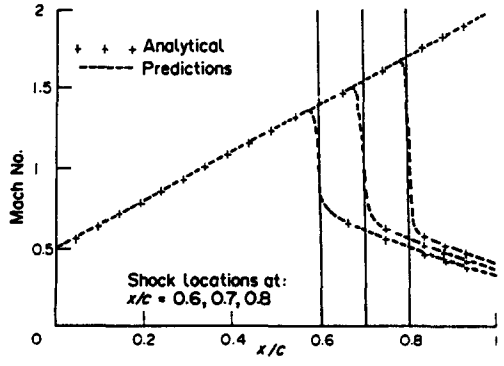

FIG. 9. Mach number distributions in a nozzle for four different back pressures.

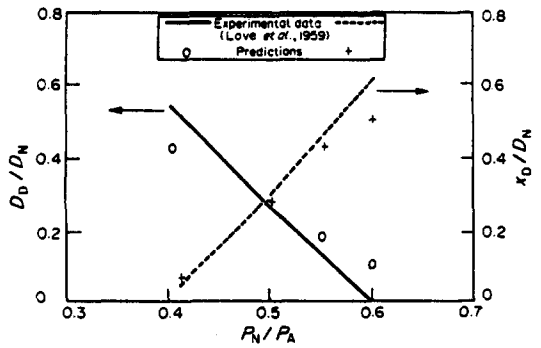

FIG. 10. Diameter and location of the Mach discs as a function of static pressure ratio.

are found. The radial extent of the domain is taken to be 1 diameter, and the axial extent is taken to be 2.5 diameters. The calculations are performed on a mesh of 80 radial cells (with 50 cells within the nozzle) by 100 axial cells, of which 60 cells are located within one nozzle-diameter downstream. This mesh results in substantially grid-independent results.

The computed location and diameter of the Mach discs are compared with the experimental data of Love *et al.* [30] in Fig. 10. The computed results correspond to the axial location and radial extent of the sonic line. It can be seen that the predictions show the correct trends, with the Mach disc moving away from the nozzle exit and decreasing in size as the pressure ratio increases. The predictions are in very good agreement with the data except for the higher pressure ratios, where the largest discrepancies are observed. These discrepancies may be due to the absence of viscosity from the predictions. Viscous effects are likely to be important across the slip line from the triple point where high mean shear is present. However, it is likely that there are further discrepancies due to the fact that the experimental values have been deduced from shadowgraphs, which correspond to density contours and not to sonic-line values.

Finally, Fig. 11 shows the computed Mach number contours for the pressure ratios 0.42 and 0.55. The figure clearly shows the collapse of the jet boundary and the production of the oblique shock wave at the nozzle lip. This shock wave runs down towards the axis to form a Mach disc. It then reflects from the triple point and runs off to meet the jet boundary, where it is reflected as an expansion wave.

3.5. *Underexpanded free jets*

The problem considered is an axisymmetric sonic jet discharging into stagnant surroundings from a nozzle at a pressure higher than the ambient pressure. Inviscid calculations are made for three different static pressure ratios, namely 1.88, 2.32 and 3.56. All three pressure ratios fall within the range of values covered by the experiments of Gibbings *et al.* [31]. The case with the highest pressure ratio corresponds to the highly-underexpanded jet studied experimentally by Donaldson and Snedeker [32], and for this case an additional calculation is made with the k–ε model specifying a discharge intensity of 1%. The radial extent of the solution domain is 1 diameter and the downstream boundary is located 4.5 diameters from the nozzle. The calculations employ a mesh of 30 radial cells, with 20 cells within the nozzle, and 100 axial cells, of which 80 cells are located within the first three nozzle diameters.

For the jet with a pressure ratio of 3.56, Fig. 12 presents the computed Mach number distribution along the jet axis, whilst the predicted Mach number contours are shown in Fig. 13. The first of these figures includes the Mach disc locations determined experimentally by Donaldson and Snedeker [32] and the predictions obtained with the inviscid and the k–ε model calculations. The figures show a rapid initial expansion of the nozzle fluid, as was observed in the experiments. For the viscous calculation, the Mach number on the centre-line is 3.4 just upstream of the first Mach disc and 0.56 just downstream of the shock. These values are in reasonable agreement with the respective values of 3.5 and 0.5 reported by Donaldson and Snedeker. The strength of the shock accords closely with that given by inviscid normal shock theory.

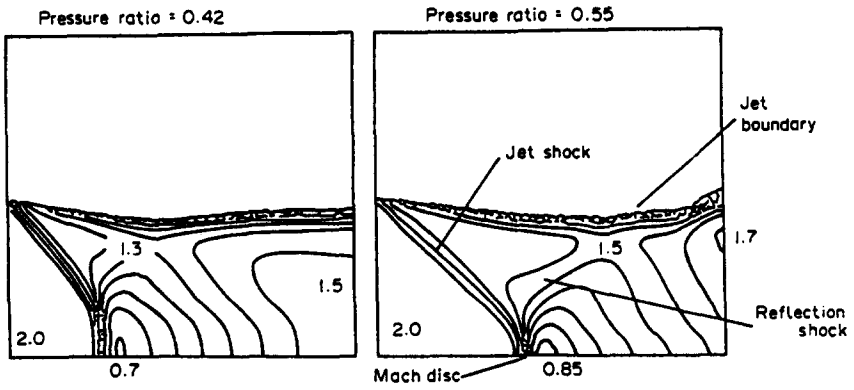

FIG. 11. Mach number contours for two different static pressure ratios in overexpanded jets.

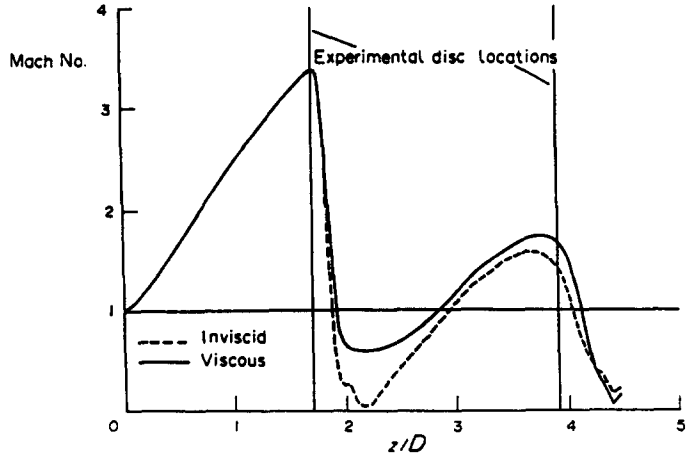

FIG. 12. Mach number distribution along the flow axis for a static pressure ratio of 3.56.

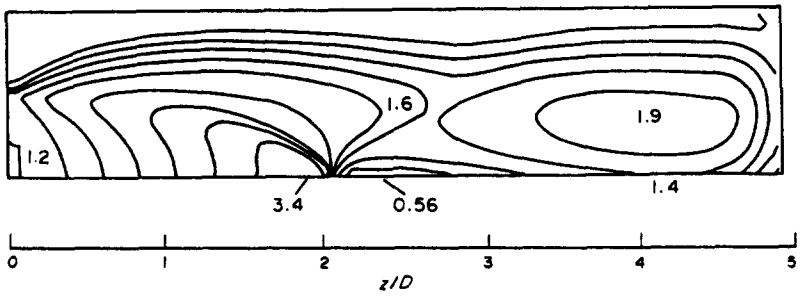

FIG. 13. Mach number contour distribution for an underexpanded jet with a static pressure ratio of 3.56.

In agreement with experiment, the model predicts the presence of two Mach discs. However, it can be seen that both discs lie somewhat downstream of the experimental locations. The solution mesh is rather coarse in the vicinity of the second disc and, in addition, the exit plane is rather close. The over-prediction of the first shock position may be due partly to insufficient grid cells in the vicinity of the disc. Figure 12 shows that the region behind the disc is sensitive to the turbulent mixing processes occurring along the slip line which trails from the triple point. These processes transport higher momentum fluid into the region behind the disc, thereby altering the pressure levels from those occurring in the inviscid calculation.

The Mach number contours depicted in Fig. 13 show that the computed structure of the jet is in good accord with that observed in experiments. As the fluid leaves the nozzle, the pressure mismatch generates a rapid expansion and a down-running oblique shock wave. This shock interacts with the expansion waves returning from the flow axis to form a Mach disc. The shock then reflects from the triple point and moves off towards the jet boundary, where it is reflected as an expansion wave. Subsequently, the flow is again accelerated and the jet becomes fully supersonic at the start of the second shock 'cell'.

Figure 14 shows the computed and measured intersections of the jet shock with the flow axis as a function of the operating pressure ratio. According to the experiments of Gibbings *et al.* [31], oblique shock reflection should occur for a static pressure ratio less than 1.83, and Mach disc intersection for a ratio greater than this value. The predictions indicate that regular reflection occurs at a ratio of 1.88, and as

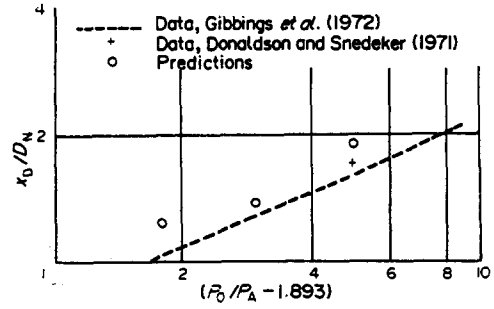

FIG. 14. Intersections of the jet shock with the flow axis as a function of pressure ratio.

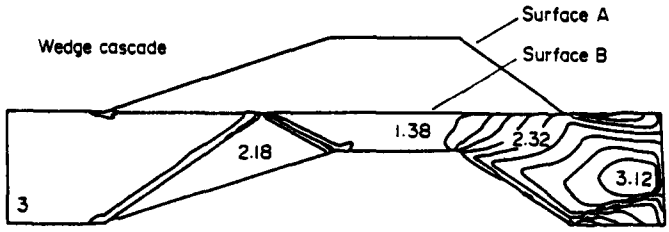

FIG. 15. Mach number contour distribution in a cascade of wedges.

may be seen from the figure, the intersection occurs somewhat downstream of the measured location. For a static pressure ratio of 2.32, it can be seen that the predicted disc location agrees very well with the measurement.

3.6. *Supersonic flow in a cascade of wedges*

The problem considered is two-dimensional supersonic flow through a cascade of wedges. The wedge cascade has a chord of 4 units, a solidity ratio of 0.25, and a leading-edge angle of 18.5°. The flow enters the cascade axially with a Mach number of 3, and throughout the cascade the flow is completely supersonic. Periodicity conditions are applied outside of the cascade. Inviscid calculations are performed on a mesh of 45 lateral cells by 168 axial cells, of which 150 cells are located in the blade row. This mesh size was found to produce solutions which for practical purposes could be considered to be grid independent.

The computed Mach number contours are shown in Fig. 15. It can be seen that the flow structure comprises a leading-edge oblique shock which reflects from the upper surface to be cancelled at the upstream corner giving uniform flow between the parallel surfaces and an expansion off the downstream corner.

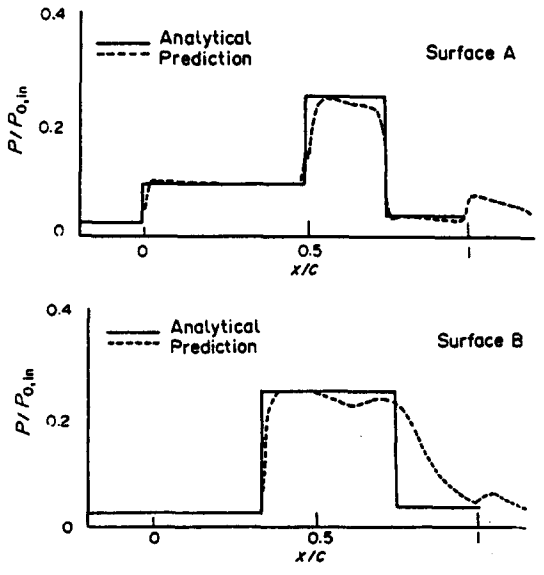

FIG. 16. Normalized static pressure distributions along each surface of the wedge.

At the trailing edge of the cascade, two compression waves are formed. The reflection of the leading-edge shock is not cancelled exactly due to numerical smearing. Consequently, a weak expansion wave emanates from the upstream corner.

Figure 16 compares the computed surface pressure distribution with those calculated from shock and expansion theory. The values are normalized with respect to the inlet total pressure and the chord respectively. For both surfaces, it can be seen that the predictions are in good overall agreement with the analytical solutions. In particular, the strengths of the oblique shock waves are predicted almost exactly. The computed static-pressure distribution on the inner surface clearly shows the weak expansion at the upstream corner, which, as was mentioned earlier, is a consequence of incomplete wave cancellation.

4. CONCLUSIONS

A numerical model was developed to simulate the characteristics of transonic and supersonic flow fields. A series of test cases including both bounded and unconfined flow was considered for its validation. Solutions were obtained of the steady-state Euler equations and then compared with available analytical results, whilst the effect of viscosity was accounted for through the solution of the full Navier–Stokes equations for comparison with existing experimental data. Good agreement was found for all the cases considered in the present study. The modifications incorporated into the model to ensure momentum and energy conservation through the shock waves proved to be particularly important in confined flows, where they lead to an accurate prediction of the shock position and strength.

Acknowledgement—The authors wish to thank Steven Dempsey of CHAM Ltd for his interest and help in this work.

REFERENCES

1. A. K. Singhal, Flow in axial turbomachinery cascades, Ph.D. Thesis, University of London (1977).
2. J. D. Denton, An improved time-marching method for turbomachinery flow calculations. In *Numerical Methods in Aeronautical Fluid Dynamics* (Edited by P. L. Roe), pp. 189–210. Academic Press, London (1982).
3. M. G. Hall, Advances and shortcomings in the cal-

culation of inviscid flows with shock waves. In *Numerical Methods in Aeronautical Fluid Dynamics* (Edited by P. L. Roe), pp. 33–60. Academic Press, London (1982).
4. A. Lerat and J. Sides, A new finite-volume method for the Euler equations with applications to transonic flows. In *Numerical Methods in Aeronautical Fluid Dynamics* (Edited by P. L. Roe), pp. 245–288. Academic Press, London (1982).
5. A. Lerat and J. Sides, Implicit time-dependent methods for the solution of the Euler equations, *VKI Lecture Series on Computational Fluid Dynamics*, 1984–04. VKI, Rhode-St-Genese, Belgium (1984).
6. D. Jespersen, Recent developments in multi-grid methods for the steady Euler equations, *VKI Lecture Series on Computational Fluid Dynamics*, 1984–04. VKI, Rhode-St-Genese, Belgium (1984).
7. G. Moretti, Computation of flows with shocks, *Ann. Rev. Fluid Mech.* **19**, 313–337 (1987).
8. P. K. Khosla and H. T. Lai, Global relaxation procedure for compressible solutions of the steady-state Euler equations, *Comput. Fluids* **15**, 215–228 (1987).
9. AGARD CP 412, Application of computational fluid dynamics in aeronautics (1985).
10. I. K. Jennions, The impingement of axisymmetric supersonic jets on cones, Ph.D. Thesis, University of London (1980).
11. W. N. Dawes, A numerical analysis of the three-dimensional viscous flow in a transonic compressor rotor and comparison with experiment, *ASME J. Turbomachinery* **109**, 83–90 (1987).
12. H. I. Rosten and D. B. Spalding, *The PHOENICS Reference Manual for Version* 1.4, CHAM TR/200 (see also CHAM/TR/100). CHAM Ltd, London (1987).
13. W. P. Jones, Models for turbulent flows with variable density, *VKI Lecture Series* 1979–2, Belgium (1979).
14. W. Rodi, *Turbulence Models and Their Applications in Hydraulics—A State of the Art Review*. Book Pub., Delft, The Netherlands (1980).
15. B. E. Launder and D. B. Spalding, The numerical computation of turbulent flows, *Comput. Math. Appl. Mech. Eng.* **3**, 269–289 (1974).
16. W. P. Jones and B. E. Launder, The prediction of laminarisation with a two-equation model of turbulence, *Int. J. Heat Mass Transfer* **15**, 301–314 (1972).
17. C. K. Lam and K. Bremhorst, A modified form of the k–ε model for predicting wall turbulence, *J. Fluid Engng* **103**, 456–460 (1981).
18. D. Vandromme and H. HaMinh, Turbulence modelling for compressible flows, *VKI Lecture Series* 1985–2, Belgium (1985).
19. M. R. Malin and L. S. Sanchez, One-dimensional steady transonic shocked flow in a nozzle, *PHOENICS J.* **1**, 214–246 (1988).
20. H. I. Rosten and D. B. Spalding, *The PHOENICS Equations*, CHAM/TR/99. CHAM Ltd, London (1987).
21. S. V. Patankar and D. B. Spalding, A calculation procedure for heat, mass and momentum transfer in three-dimensional parabolic flows, *Int. J. Heat Mass Transfer* **15**, 1787–1805 (1972).
22. D. B. Spalding, Four lectures on the PHOENICS computer code, CFD/82/5, CFDU, Imperial College, University of London (1982).
23. H. L. Stone, Iterative solution of implicit approximation of multi-dimensional partial differential equations, *SIAM J. Numer. Analysis* **5**, 530 (1968).
24. H. I. Rosten and D. B. Spalding, *PHOENICS Reference Handbook: Advance Copy*, CHAM/TR/100. CHAM Ltd, London (1985).
25. J. Viegas and M. Rubesin, Wall-function boundary conditions in the solution of the Navier–Stokes equations for complex compressible flows, AIAA Paper No 83-1964 (1983).
26. A. Palacio and M. R. Malin, Simulation of supersonic flow past a double-wedge profile, *PHOENICS J.* **1**, 371–408 (1989).
27. A. H. Shapiro, *The Dynamics and Thermodynamics of Compressible Flow*, Vol. 1. Ronald Press, New York (1953).
28. F. Villasenor and D. Radosavljevic, Numerical simulations of flat plate turbulent boundary layer in supersonic flow, *PHOENICS J.* **1**, 141–213 (1988).
29. M. R. Malin, Calculation of two-dimensional flow in axial turbomachinery cascades, M.Sc. Thesis, University of London (1977).
30. G. S. Love, C. E. Grigsby, L. P. Lee and M. J. Woodling, Experimental and theoretical studies of axisymmetric free jets, NACA TR R6 (1959).
31. J. C. Gibbings, J. Ingham and D. Johnson, Flow in a supersonic jet expanding from a convergent nozzle, ARC CP No. 1197 (1972).
32. C. Donaldson and R. S. Snedeker, A study of free-jet impingement. Part 1. Mean properties of free and impinging jets, *J. Fluid Mech.* **45**, 281–319 (1971).

CALCUL NUMERIQUE DES CHAMPS D'ECOULEMENTS PERMANENTS TRANSONIQUES ET SUPERSONIQUES

Résumé—Une procédure de calcul des ondes de choc ou de détente est présentée pour les écoulements transoniques ou supersoniques. De façon à connaître la validité du modèle, les calculs sont faits pour des cas dont les solutions analytiques ou les données sont publiées. Les cas considérés sont: jet supersonique, écoulement supersonique dans une cascade d'aubes avec réflexion d'onde de choc et onde de détente de Prandtl–Mayer. Le modèle qui inclut la solution permanente des équations d'Euler aussi bien que les équations complètes de Navier–Stokes, utilise une formulation de volume fini modifiée pour assurer la conservation de la quantité de mouvement et de l'énergie à travers l'onde de choc. Dans tous les cas, les calculs s'accordent bien avec les résultats analytiques et expérimentaux.

NUMERISCHE BERECHNUNG STATIONÄRER SCHALLNAHER UND ÜBERSCHALLSTRÖMUNGSFELDER

Zusammenfassung—Es wird ein Verfahren zur Berechnung der Stoß- und Expansionswellen bei Strömungen im Bereich der Schallgeschwindigkeit und des Überschalls vorgestellt. Um die Zuverlässigkeit des Modells abzuschätzen, wird eine Reihe von Sonderfällen durchgerechnet, für die analytische Lösungen oder Versuchsdaten vorliegen. Folgende Fälle werden betrachtet: Überschallströmung an Strahlrudern, schallnahe Strömungen mit Verdichtungsstoß in einer Düse, über- und unterexpandierte Freistrahlströmungen mit der Ausbildung einer "Mach-Scheibe" und schließlich eine Überschallströmung mit einer Abfolge von Stoßreflexionen und Prandtl–Meyer-Expansionen. Das Modell berücksichtigt die Lösung der stationären Euler-Gleichungen wie auch der vollständigen Navier–Stokes-Gleichungen. Ein bestehendes Finite-Volumina-Verfahren wird modifiziert, um die Erhaltung von Impuls und Energie über den Verdichtungsstoß zu gewährleisten. In allen Fällen zeigen die Berechnungen eine gute Übereinstimmung mit analytischen und experimentellen Ergebnissen.

ЧИСЛЕННЫЕ РАСЧЕТЫ ПОЛЕЙ СТАЦИОНАРНЫХ ОКОЛОЗВУКОВОГО И СВЕРХЗВУКОВОГО ТЕЧЕНИЙ

Аннотация—Описывается процедура расчета ударных волн и волн разрежения, связанных с околозвуковым и сверхзвуковым течением. С целью оценки способности модели проведены вычисления для ряда точек расчета, для которых существуют аналитические решения или опубликованы данные. Рассмотрены следующие случаи: сверхзвуковое течение над лопатями реактивного двигателя, околозвуковое течение со скачком уплотнения в сопле, перерасширенные и недорасширенные свободные струи с образованием дисков Маха, а также звуковое течение в каскаде клиньев с отражением скачка уплотнения и расширением Прандтля–Мейера. В модели, включающей решение стационарных уравнений Эйлера, а также полных уравнений Навье–Стокса, используются некоторые модификации существующей формулировки конечных объемов для обеспечения сохранения импульса и энергии в ударных волнах. Во всех случаях расчеты удовлетворительно согласуются с аналитическими и экспериментальными данными.